

## COLD Activity Report- year 2023

D. Alesini, P. Albicocco, D. Babusci, M. Beatrice (Tecn.), M. Beretta, B. Buonomo, A. Calanca (Tecn.), F. Chiarello (CNR-IFN), D. Di Bari(Tecn.), A. D'Elia (AR), L. Foggetta, G. Felici, M. Gatta(Tecn.),D. Di Gioacchino, C. Gatti, C. Ligi, G. Maccarrone, F. Mattioli (CNR-IFN), G. Papalino(Tecn.), L. Piersanti,G. Pileggi (Tecn.), A. S. Piedjou Komnang (AR), A. Rettaroli (AR), G. Torrioli (CNR-IFN), S. Tocci (TD)

### 1 Characterization of a Transmon in 3D cavity: first measurements of individually resolved photons in Italy

Quantum computation is nowadays one of the most attractive areas of research. The main advantage of quantum computation over classical computation resides in the qubit as the quantum equivalent of the binary logical bit. Among the many qubit types, superconducting qubits based on Josephson junctions (JJs) are the most promising since they can be printed on substrates like silicon electronics, retaining great scalability potential. JJs are versatile superconducting devices that can be used for many cutting edge applications such as microwave photon detection, parametric amplification, and entangled photon emission. We studied a transmon qubit coupled dispersively to a 3D resonant cavity [1]. The device was tested at LNF in a Leiden Cryogenics CF-CS110-1000 dilution refrigerator on the 10 mK plate. The qubit was fabricated at the technology and Innovation Institute in Abu Dhabi. We investigated the transmon-cavity system using spectroscopic techniques allowing us to count single photons inside the cavity for the first time in Italy [2].

We studied the system response in the time domain performing Rabi and Ramsey spectroscopy to study the qubit coherence properties obtaining  $T_1 = 8.68 \pm 0.72 \mu\text{s}$ ,  $T_2 = 2.30 \pm 0.11 \mu\text{s}$  and  $T_\phi = 2.65 \pm 0.15 \mu\text{s}$  [2].



Figure 1: **(Left)**: Al cavity hosting the transmon chip. **(Right)**: optical image of the transmon shunt capacitance pads acquired with a 50 $\times$  magnification. The JJ is located between the pads.

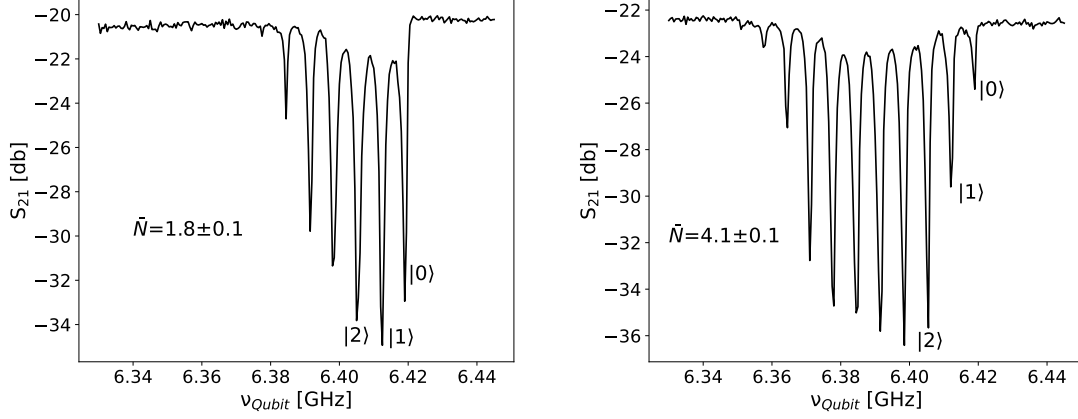


Figure 2: Qubit spectroscopy of individually resolved photon numbers inside the cavity, for an average photon population of  $\bar{N} = 1.8$  (**left**,  $P_{probe} = -102$  dbm) and  $\bar{N} = 4.1$  (**right**,  $P_{probe} = -98$  dbm). Each peak is separated by  $2\chi/2\pi = -6.82 \pm 0.16$  MHz.

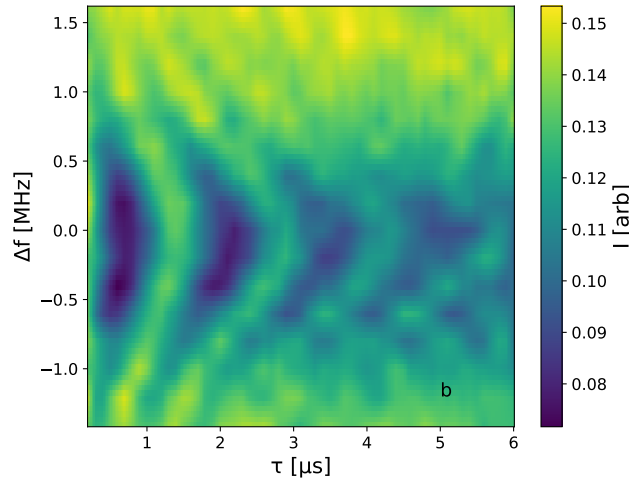


Figure 3: Chevron plot, acquired with excitation power  $P = -93$  dbm. The y-axis is given as detuning from the resonance frequency of 6.4194 GHz.

## 2 Optimized design and simulation of 3D Transmon

Transmon qubits are susceptible to various sources of noise contributing to the decrease of the qubit coherence time. We exploit electromagnetic simulations in ANSYS [3] to design a transmon qubit where the electromagnetic losses are minimized. Electromagnetic losses are defined by the sum of the participation ratios contributions from different spatial regions of the chip. We started from the transmon design of [2] and modified the shape and size of the capacitive pads. We adjusted the geometric parameters and explored other simple geometric shapes of the pads. Analyzing

the distribution of the electromagnetic fields, we observed that a significant portion of the field concentrated on the corners of the pads, leading to an increase in total electromagnetic losses. We smoothed the corners of the pads and added non-straight lines to increase the area, achieving a more homogeneous distribution of the field. A geometry with two circular pads resulted to be the most suitable to minimize electromagnetic losses. The distribution of the electric field on the qubits is shown in figure 4. The pads are circles of radius  $500 \mu\text{m}$  with a distance of  $543 \mu\text{m}$  between the center of the pad and the center of the JJ. The junction has dimension  $2 \times 2 \mu\text{m}^2$  with an inductance  $L_J = 7.8 \text{ nH}$ , corresponding to a critical current  $I_c = 42 \text{ nA}$ . The total capacity is  $C = 93 \text{ fF}$  and the qubit-cavity coupling is  $g_{01} = 355 \text{ MHz}$ . The estimated relaxation time is  $T_1 = 63 \mu\text{s}$ . The larger dimensions of the pads allow for a smoother distribution of the electromagnetic field, resulting in a significant reduction in losses. The estimation of the electromagnetic losses can be improved optimizing the simulation design. We are currently adjusting the mesh resolution to improve the accuracy of the loss values.

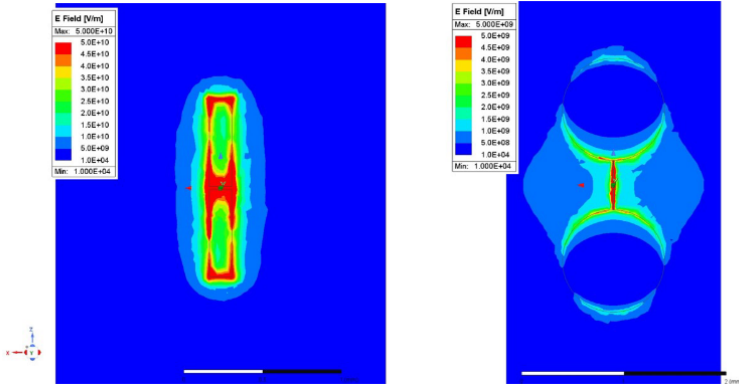


Figure 4: Electric fields distributions for a transmon with rectangular pads (left) and circular pads (right).

The first prototypes of the transmon with circular pads have been produced by CNR-IFN. We plan to test the newly designed qubit in the forthcoming months.

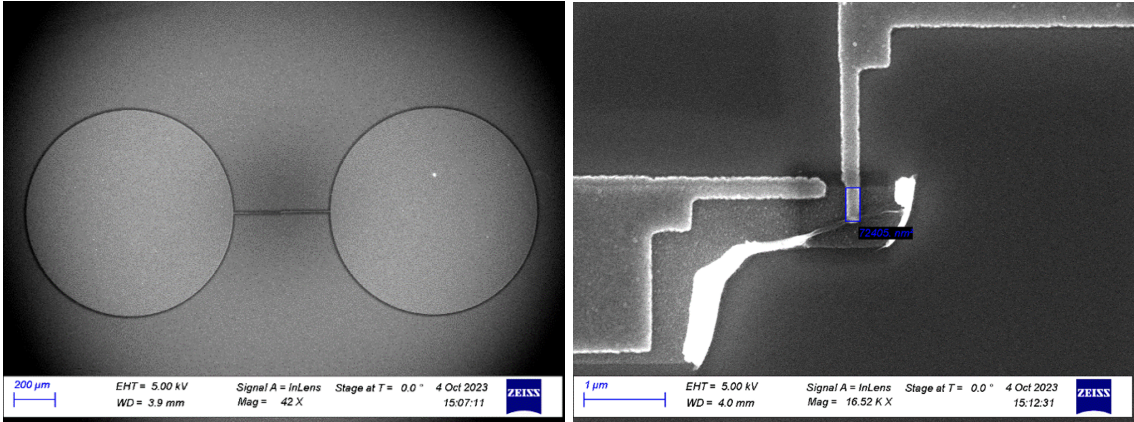


Figure 5: SEM images of the Transmon with circular pads.

Table 1: Capacitance values extracted with Ansys Q3D.

$C_s$ Qubit shunt	$C_c$ Qubit-bus coupling	$C_g$ Qubit-readout coupling
83.92 $fF$	1.9462 $fF$	4.643 $fF$

### 3 Design of a 2D qubit coupled to a quantum bus

We studied two transmon qubits coupled through a quantum bus. This kind of devices are suitable to exploit Quantum Non Demolition (QND) technique to develop a photon counter based on superconducting qubits for fundamental physics. Within the INFN Qub-IT and PNR project we developed a first design consisting on a 2D transmon qubit which is coupled to a transmission line through a  $\lambda/4$  resonator [4]. We scaled up the system to a circuit made up of two qubits entangled via a quantum bus. The design of the two qubits device is realized using the Qiskit-Metal open-source software developed by IBM [5]. The analyses of the circuit Hamiltonian of our system are done using the EPR (Energy Participation Ratio) and the LOM (Lumped Oscillator Model) techniques.

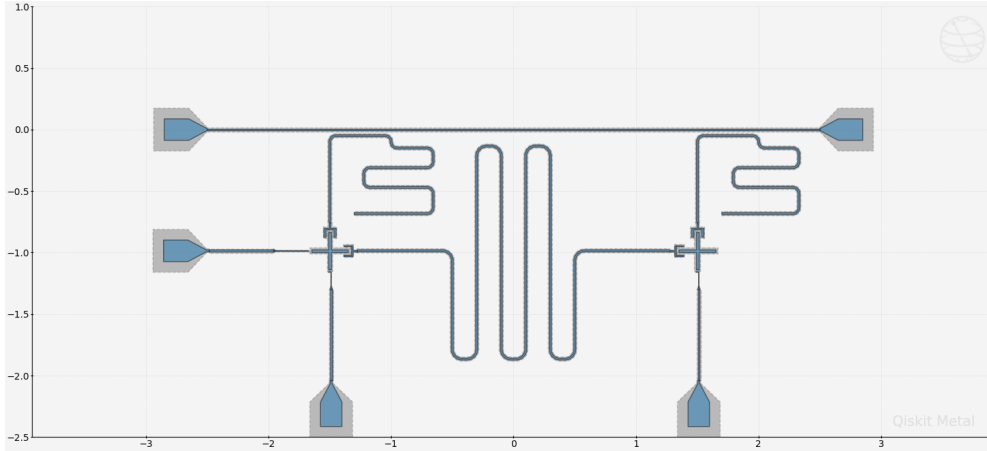


Figure 6: Design in Qiskit-Metal of the two Xmon coupled via a quantum bus.

In Figure 6 we show the rendering in Qiskit-Metal of our circuit that consists of two Xmon-type qubits capacitively coupled to a bus resonator ( $\lambda/2$ ). Each of the two Xmon qubits is also capacitively coupled to a quarter-wave readout resonator, 3.76mm and 3.67mm long, respectively. The Xmons are designed with the same parameters: each of their electrodes are 21 $\mu m$  wide and 150 $\mu m$  long. The half-wave bus resonator is 10.82mm long, with 15 $\mu m$  trace width and 9 $\mu m$  gap. The readout resonators are capacitively coupled to the 500 $\mu m$  transmission line. The design is made in such a way the qubits are far detuned from the bus resonator.

Performing simulations using Ansys Q3D and Ansys HFSS [3], we are able to extract some Hamiltonian parameters such as resonant frequencies, anharmonicity and the qubit-bus-qubit coupling. Ansys Q3D is used to extract the coupling capacitance values of our system. The simulated values summarized in Table 1 are valid for both qubits.

For the other parameters of the system, we refer to LOM and EPR analyses for a wide range of JJ inductance. In Fig 7 we plot the qubit frequencies as a function of junction inductance.

The LOM and EPR simulations for  $L_J = 10nH$  are in agreement. At this specific value, we get  $freq_{EPR}/2\pi = 4.91GHz$ ,  $freq_{LOM}/2\pi = 4.97GHz$  and  $freq_{readout}/2\pi = 7.45GHz$ .

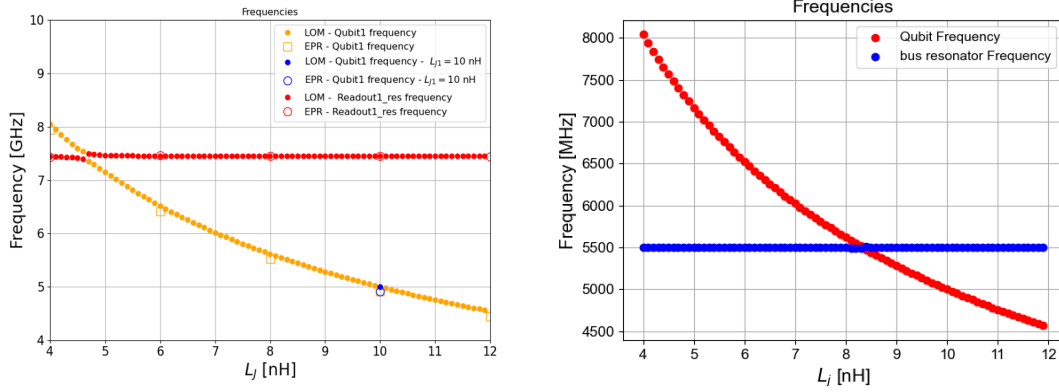


Figure 7: (Left) Qubit frequency as a function of Josephson junction inductance  $L_J$  considering the readout resonator. The simulations are done with LOM and EPR methods and for a specific Josephson junction inductance  $L_J = 10nH$ . (Right) Qubit frequency as a function of Josephson junction inductance  $L_J$  considering the bus resonator.

The dispersive shift as a function of the detuning (both for readout and bus resonator) is shown in Fig. 8. For  $L_J = 10nH$ , we get an agreement between the LOM and EPR simulations and  $\chi_{EPR}/2\pi = -0.307MHz$  and  $\chi_{LOM}/2\pi = -0.312MHz$ .

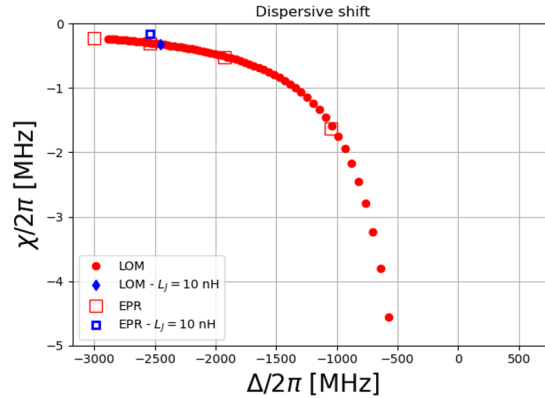


Figure 8: Dispersive shift as a function of detuning considering the readout resonator. The simulations are done with LOM and EPR methods and for a specific Josephson junction inductance  $L_J = 10nH$ .

We analyse also the case when we sweep one of the Josephson junction qubit's inductance and keep fixed the value of the other qubit and the qubits are coupled only with the bus resonator, see Fig 9.

In Fig 10 we show, from the EPR analyses, the frequency as a function of qubit Josephson junction inductance. We observed that, at  $L_{J1} = 10nH$ , both qubits frequencies are more or less the same as calculated.

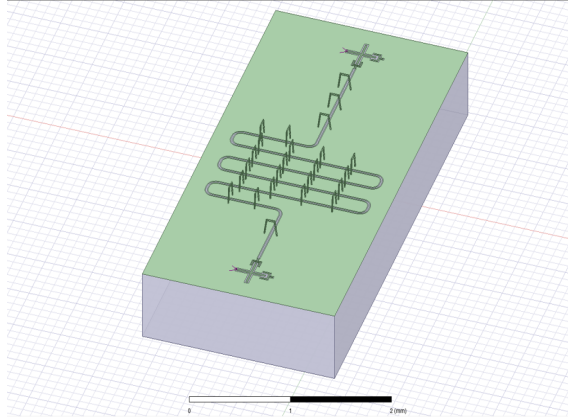


Figure 9: The two qubits coupled with the bus resonator rendered in Ansys.

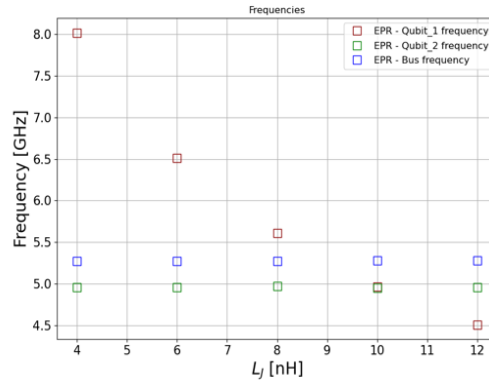


Figure 10: Frequency of the qubits as a function of  $L_{J1}$ .

This work is still in progress to fully characterize our system parameters and proceed to fabrication and measurements.

#### 4 Improved characterization of the T-type Superconducting Quantum Network detector with 10 qubits

A Superconducting Quantum Network (SQN) could be used to improve the detection sensitivity to single microwave photons. We tested at LNF within the Supergalax project a SQN working as a coupling element between two perpendicular resonators. The advantage of using a SQN over a single qubit is that of a predicted scaling of the signal-to-noise ratio as the number of qubits  $N$  instead of  $\sqrt{N}$ .

Following a discussion with the theory group of the Supergalax project on the results obtained on the T-type SQN device [6], we repeated at LNF the characterization of the same device with the goal of studying the dependency of the transmission  $S_{21}$  from both power and frequency of the second “pump” tone, bias magnetic field and then searching the presence of hysteresis in the effect. The main result, is the dependence on the pump frequency, and not only on the power, of the resonant drop in the transmission spectrum ( $S_{21}$ ) shown in the left panel of Fig. 11. In

the right panel we compare the observed trends, with the pump frequency at 7.743 GHz, while increasing (blue line) or decreasing (red line) the power, showing a hysteresis which is interpreted as a proxy of bistability.

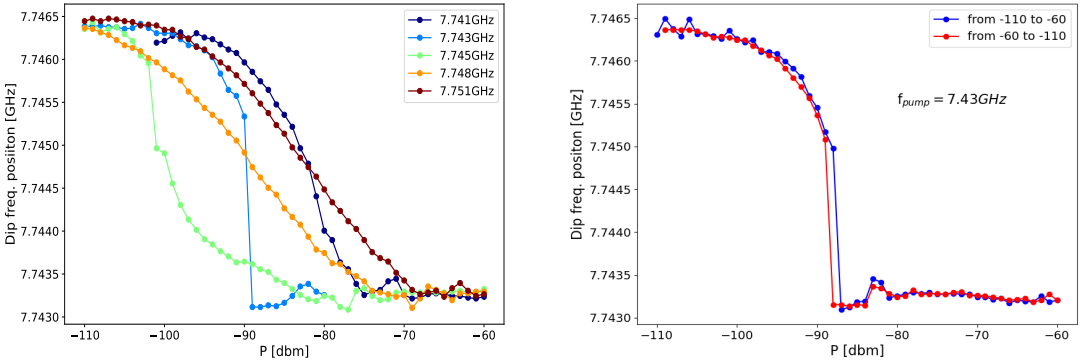


Figure 11: (Left) Peak position of the resonant drop in the transmission spectrum for different power and frequencies of the pump signal. (Right) Peak position of the resonant drop in the transmission spectrum as a function of the pump power. Hysteresis is observed when rising or lowering the power.

We applied an external magnetic field to the circuit by an external coil wound around the sample holder with  $B/I = 1$  Gauss/35 mA. In Fig. 12 we show the variation of the transmission spectrum  $S_{21}$  for different applied magnetic fluxes. The pump tone was kept at the resonant point at 7.74328 GHz with power -90 dbm. By varying the voltage applied to the coil circuit, where one applied flux quantum corresponds to about few volts, we observe a 20 db variation of the transmission drop (left panel) compatible with a stronger coupling to the qubits. The effect seems to have the right periodicity even if induced heating at higher bias current precluded further investigation.

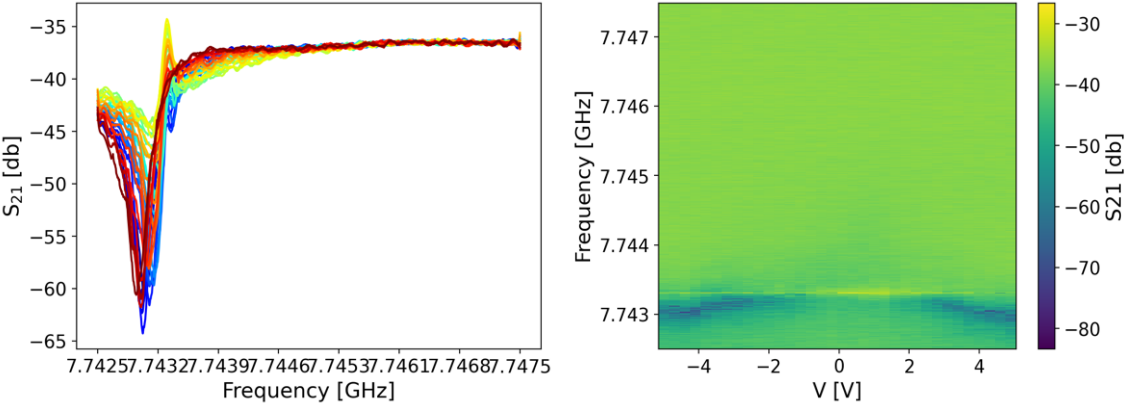


Figure 12: Variation of the transmission spectrum  $S_{21}$  as a function of the applied magnetic flux (4Volts about one flux quantum  $\Phi_0$ ) with pump frequency 7.74328 GHz and power -90 dbm.

## 5 Dart Wars

Noise at the quantum limit over a large bandwidth is a fundamental requirement for challenging future applications, especially for dark matter and axion detection. Resonant axion-detectors, such as haloscopes, must probe a range of frequencies of several GHz keeping the system noise to the lowest possible level. To this end, devices called traveling wave parametric amplifiers (TWPAs) are currently being developed. The nonlinear element of TWPAs is provided by arrays of JJ or by the kinetic inductance of a high-resistivity superconductor. In the framework of the Dart Wars project (funded by CSN 5 of INFN), we tested at LNF a TWPA produced by the INRIM. The TWPA was tested on the 10 mK plate of our Leiden dilution refrigerator. We measured the scattering parameter of this device as a function of the bias current as reported in figure 13. We observe a modulation of the transmission properties of the device with a period of about  $46 \mu A$ . We were not able to find the condition for any wide-band amplification. However we managed to observe single point signal amplification (about 8 dB), for  $I_{bias}=0 \mu A$ ,  $f_{pump} = 7.74727$  GHz,  $P_{pump} = 4.5$  dBm.

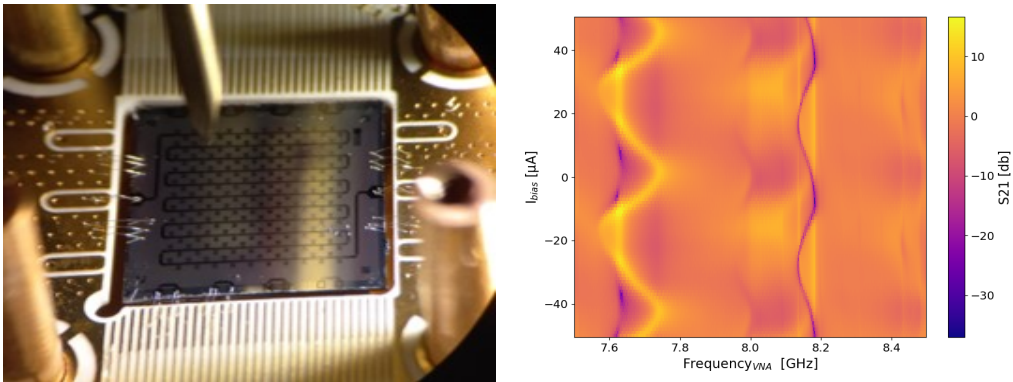


Figure 13: (Left) Optical image of the TWPA chip bonded to the sample holder. (Right) Trend of the TWPA,  $S_{21}$  scattering parameter as a function of the bias current.

## 6 Microwave photon emission in superconducting circuits

Josephson Junction (JJ) based devices yield great potential for entangled photon generation [7]. The interest in entangled photons emitters lies in their potential to enable new types of quantum technologies, like secure quantum communication, and error correction in quantum computing [8]. Within the PNR MUR project NQSTI, JJ, a SQUID and a JTWPA (Josephson traveling wave parametric amplifier) as microwave emitters [9]. We studied the emission spectra of these superconducting circuits when excited by a direct pump. We identified two regions of the spectra that can be modelled with two different approaches. The low pump-power region can be modelled by a dynamic Casimir effect, while the high power region by an Autler-Townes emission stimulated by two photon processes [9].

As further development we aim to study the entanglement properties of the photons generated by these devices.

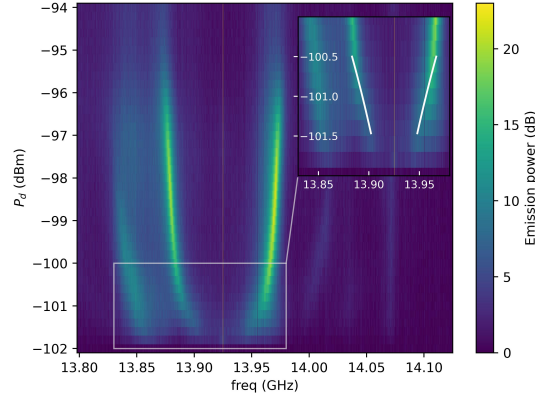


Figure 14: SQUID responses to the applied pump drive tone. The x-axis is the frequency range scanned by the spectrum analyzer, while the colorbar indicates the intensity of the spectrum with respect to the background. The figure shows a collection of spectra as a function of drive power (y-axis) at a fixed drive frequency of 13.925 GHz. The inset shows a zoomed view of the linear regime; here, the white lines indicate the simulation results following the calculations of Appendix ??.

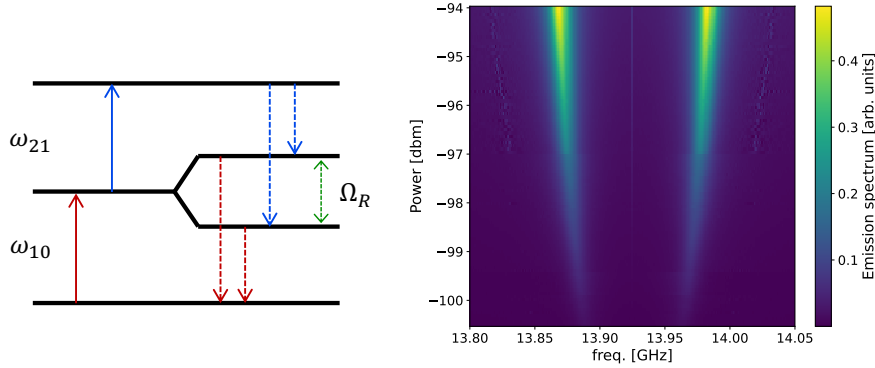


Figure 15: *Left*): Illustrative energy levels diagram for the Autlers-Townes transitions for the SQUID. The energy spacing in this diagram are magnified for illustrative purpose. In our model we included an additional fourth undressed state, that is not depicted here for sake of clarity. *Right*): Simulated Autler-Townes emission spectrum of the SQUID.

## 7 Superconducting resonant cavity

Within QUAX, we search for axion using an haloscope. It consists of a resonant cavity immersed in a strong magnetic field. This usually reduces the quality factor, thus hindering the detection potential of the haloscope. To prevent this phenomenon, we are carrying on an R&D to use alternative superconductors with high  $H_{c2}$  to build resonant cavities. This R&D is ongoing now within the SAMARA and SQMS projects. We tested a Nb cavity, coated with a film of  $Nb_3Sn$  (about  $3 \mu\text{m}$  thick).  $Nb_3Sn$  has a  $H_{c2}$  of about 18 T, thus it is a very good candidate to reduce the detrimental effect of the magnetic field on the quality factor of a resonant cavity. The cavity has been fabricated @ FERMILAB, chicago USA and it has been tested at LNF. For the characteri-

zation, the Nb<sub>3</sub>Sn cavity has been mounted on the 10 mK stage of our Leiden Cryogenics dilution refrigerator. We assured that the cavity axis was aligned perpendicularly to the 10 mK plate, to have it parallel to the magnetic field axis. We measured the scattering parameters S<sub>21</sub> and S<sub>11</sub> to extract the loaded and unloaded quality factor. The experimental data are reported in figure 16.

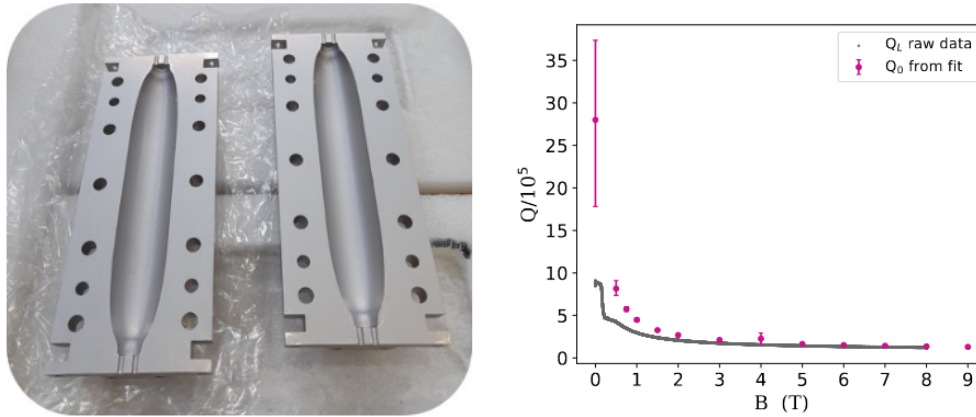


Figure 16: *Left*): Resonant cavity coated with Nb<sub>3</sub>Sn. *Right*): Trend of  $Q_0$  and  $Q_L$  as a function of the applied magnetic field.

This cavity was able to withstand a magnetic field of 9 T retaining a  $Q_0$  of about 120000. We expect that improving the quality of the Nb<sub>3</sub>Sn coating (i.e. stoichiometry and phase purity), also the quality factor will improve. We also tested the performances in magnetic field of a Cu cavity covered with REBCO tape. REBCO is a high T<sub>c</sub> superconductor with an  $H_{c2} \approx 100$  T. The Cu cavity was produced at LNF, while the REBCO tape was assembled on the cavity at ENEA (Frascati). Also in this case we measured the scattering parameters and extracted the quality factor of the cavity. The measurements were performed in an homemade cryostat equipped with a 8 T magnet. During the measurements the cavity was kept at 4.2 K.

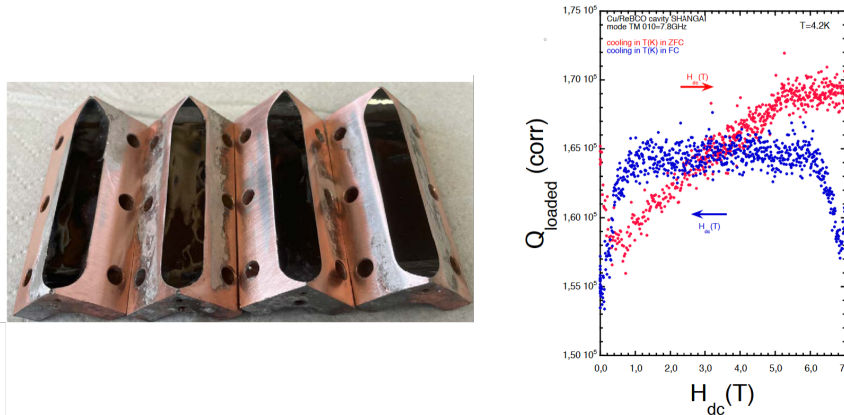


Figure 17: *Left*): Resonant cavity covered with REBCO tape. *Right*): Trend of  $Q_L$  as a function of the applied magnetic field.

For this cavity the Quality factor is essentially stable at a value of 160000. We believe that improving the process we use to glue the REBCO tape to the cavity wall, can provide better

performances for the next prototype of cavity.

## 8 RESILIENCE: Magnetic field resilient microwave single photon detector based on van der Waals Josephson junctions

RESILIENCE is young researcher project founded by the CSN5 of INFN. Its purpose is that of using NbSe<sub>2</sub> to fabricate JJ. NbSe<sub>2</sub> is a van der Waals material that is able to withstand magnetic field as high as 30 T. A JJ made of NbSe<sub>2</sub> would inherit its magnetic field resiliency and could be used as single photon counter. Thus fabricating JJ made of NbSe<sub>2</sub> would be extremely beneficial for experiments like QUAX where a high magnetic field is coupled to the necessity of single photon counting. To fabricate NbSe<sub>2</sub> JJ we mechanically exfoliate NbSe<sub>2</sub> flakes using the standard approach proposed in [10]. We followed two parallel roads to fabricate the JJ. The sandwich like JJ (where two flakes of NbSe<sub>2</sub> are separated by a third not superconducting flake) and the Dayem bridge approach.

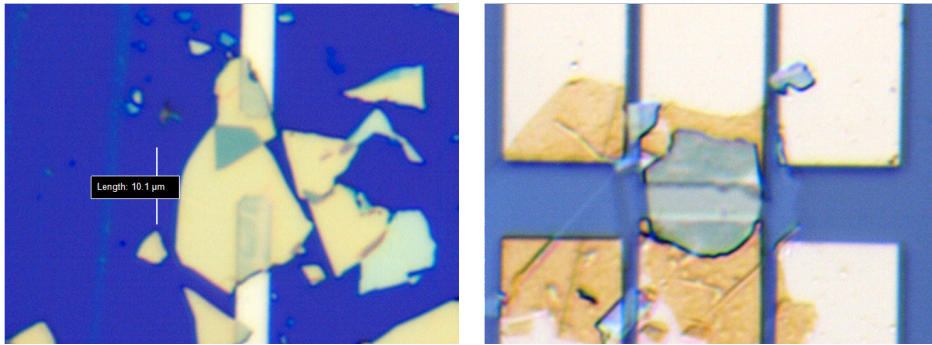


Figure 18: *Left*): Two overlapped NbSe<sub>2</sub> flakes. the superposition region manifests a different colour with respect to the individual flakes. *Right*): NbSe<sub>2</sub>/hBN heterostructure deposited over electrical contacts. This heterostructure is the precursor of the Dayem bridge.

The pre-patterned substrate with electrical contacts have been produced by IFN-CNR. We plan to test these two kind of JJ in the forthcoming year.

## 9 List of Conference Talks by LNF Authors in Year 2023

Include a list of conference talks by LNF authors.

1. A.D'Elia *RESILIENCE: Magnetic field resilient microwave single photon detector based on van der Waals Josephson junctions*. University of Camerino, Feb. 2023
2. C.Gatti *Fundamentals of quantum bits (qubit) working and its technological applications*, School of science and technology of Camerino, 10-hour seminar for PhD Physics students (1 cfu), 12-14 Mar. 2023
3. C.Gatti *Introduzione ai circuiti superconduttivi quantistici*, Seminario presso DIEM Università Roma Tre, 23-25 May 2023
4. A. D'Elia *RESILIENCE: Magnetic field resilient microwave single photon detector based on van der Waals Josephson junctions*. HTSHFF 2023, Sept. 2023

5. A. Rettaroli, (poster) *Design, fabrication and characterization of a ultra-high-Q resilient Nb3Sn resonant cavity*, Quantum Technologies for Fundamental Physics, EMFCSC, Erice - Sept. 2023
6. C.Gatti *I Qubit Superconduttivi*, Seminari di Superconduttività Applicata, IEEECS, presso il DIEM Università Roma Tre, 19 Dec. 2023

## 10 Publications

1. D'Elia, A. et al. Microwave Photon Emission in Superconducting Circuits. *Instruments* **7**, 36 (2023)
2. Gatti, C. et al. Coherent Quantum Network of Superconducting Qubits as a Highly Sensitive Detector of Microwave Photons for Searching of Galactic Axions. *IEEE Transactions on Applied Superconductivity*, **33**, 5, (2023)
3. D'Elia, A. et al. Stepping Closer to Pulsed Single Microwave Photon Detectors for Axions Search *IEEE Transactions on Applied Superconductivity*, **33**, 5, (2023)
4. Moretti, R. et al. Design and simulation of a transmon qubit chip for Axion detection *IEEE Transactions on Applied Superconductivity*, **34**, 3, (2024)
5. D'Elia, A. et al. Characterization of a Transmon Qubit in a 3D Cavity for Quantum Machine Learning and Photon Counting. *Applied Sciences* **14**, 1478 (2024).

## References

1. Koch, J. *et al.* Charge-insensitive qubit design derived from the Cooper pair box. *Physical Review A* **76**, 042319 (2007).
2. D'Elia, A. *et al.* Characterization of a Transmon Qubit in a 3D Cavity for Quantum Machine Learning and Photon Counting. *Applied Sciences* **14**, 1478 (2024).
3. *ANSYS HFSS software* <https://www.ansys.com/products/electronics/ansys-hfss>.
4. Moretti, R. *et al.* Design and Simulation of a Transmon Qubit Chip for Axion Detection. *IEEE Transactions on Applied Superconductivity* (2024).
5. Mineev, Z. K. *et al.* Qiskit Metal: An Open-Source Framework for Quantum Device Design Analysis (2021).
6. D'Elia, A. *et al.* Stepping closer to pulsed single microwave photon detectors for axions search. *IEEE Transactions on Applied Superconductivity* **33**, 1–9 (2023).
7. Esposito, M. *et al.* Observation of Two-Mode Squeezing in a Traveling Wave Parametric Amplifier. *Phys. Rev. Lett.* **128**, 153603. <https://link.aps.org/doi/10.1103/PhysRevLett.128.153603> (15 Apr. 2022).
8. Luo, Y.-H. *et al.* Quantum teleportation of physical qubits into logical code spaces. *PNAS* **118**, e2026250118. <https://www.pnas.org/doi/abs/10.1073/pnas.2026250118> (2021).
9. D Elia, A. *et al.* Microwave Photon Emission in Superconducting Circuits. *Instruments* **7**, 36 (2023).
10. Castellanos-Gomez, A. *et al.* Deterministic transfer of two-dimensional materials by all-dry viscoelastic stamping. *2D Mater. Lett* **1**, 1–8 (2014).